# Actively Tailored Spatiotemporal Images of Quantum Interference on the Picometer and Femtosecond Scales

Hiroyuki Katsuki,[1,2] Hisashi Chiba,[1,2] Christoph Meier,[3,*] Bertrand Girard,[3] and Kenji Ohmori[1,2,†]

[1]*Institute for Molecular Science, National Institutes of Natural Sciences, Myodaiji, Okazaki 444-8585, Japan*

[2]*CREST, Japan Science and Technology Agency, 1-9-9, Yaesu, Chuoh-ku, Tokyo 103-0028, Japan*

[3]*Université de Toulouse; UPS; CNRS; IRSAMC; Laboratoire Collisions, Agrégats, Réactivité; F-31062 Toulouse, France*

(Received 10 March 2008; published 11 March 2009)

Interference fringes of quantum waves weave highly regular space-time images, which could be seen in various wave systems such as wave packets in atoms and molecules, Bose-Einstein condensates, and fermions in a box potential. We have experimentally designed and visualized spatiotemporal images of dynamical quantum interferences of two counterpropagating nuclear wave packets in the iodine molecule; the wave packets are generated with a pair of femtosecond laser pulses whose relative phase is locked within the attosecond time scale. The design of the image has picometer and femtosecond resolutions, and changes drastically as we change the relative phase of the laser pulses, providing a direct spatiotemporal control of quantum interferences.

DOI: 10.1103/PhysRevLett.102.103602 PACS numbers: 42.50.Md, 33.80.−b, 82.53.Kp

The wave nature of matter is at the heart of quantum theory. It has been manifested in interferometric measurements similar to the celebrated Young's double slit experiment for light. Examples of such quantum interferometry have so far been demonstrated for the translational motion of electrons [1], atoms [2], and molecules such as fullerenes and small porphyrins [3].

Quantum interferometry has also been developed with electronic wave packets (WPs) in atoms [4–10] and rotational and vibrational WPs in molecules [11–20], based on the measurements of WP density in the bound electronic state as a function of the relative phase of twin optical pulses that produce a pair of WPs. Aside from such bound-state interferometry, WP interference has also been observed in the ionization continuum of the K atom [21] and in the continuum states above the dissociation limit of the potential curve [22].

In most of these examples of WP interferometry (WPI), two WPs move in the same direction with the same momenta so that their spatial overlap is stable in time. The situation is drastically different with counterpropagating WPs. Transient picometric standing waves called "quantum ripples" appear and disappear synchronously with the periodic crossing of two WPs [23–25]. Theory predicts that such periodic appearance and disappearance of quantum ripples will weave highly regular space-time images called "quantum carpets" [26,27] or "quantum fractals" [28], as shown in the right panel of Fig. 1. Quantum carpets are wonderful manifestations and compelling evidence for the wave nature. A similar phenomenon was already discovered in the classical world about 170 years ago by Henry Talbot for light in the Fresnel diffraction regime; this is the well-known "Talbot effect"[27]. The Talbot carpet is woven on a spatial plane instead of the space-time plane for the quantum carpet, and has recently been observed also for atomic and molecular beams [3,29]. Both of the quantum and Talbot carpets originate from the intermode interferences among different eigenwaves superposed coherently. The constant phase lines in the evolution of the interferences draw geometric images. The quantum carpet has been studied theoretically in various quantum systems such as particles in model potentials [26,27], Bose-Einstein condensates (BEC) [30], and fermions in a box potential [31], and has been observed experimentally by Deng *et al.* in BEC in 1999 [32].

In the current Letter, we present the first actively tailored quantum carpets, which have been realized by exquisitely controlling the quantum ripples in molecules. We employ

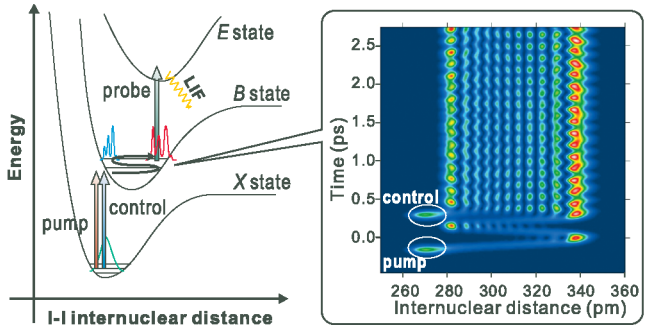


FIG. 1 (color). Pump-control-probe scheme for tailoring and visualizing the quantum carpet in the iodine molecule. (Left) Three femtosecond laser pulses are employed. Two of them are phase locked and used as the pump and control pulses, and the other one is not phase locked and is used as the probe pulse. The fluorescence signal induced by the probe pulse is measured with a photomultiplier tube attached to a monochromator. (Right) The model simulation of the quantum interference of two wave packets created on the *B*-state potential curve of the iodine molecule by the pump and control pulses. The interference shows a highly regular space-time image that looks like a carpet.

 

high-precision WPI coupled with ultrafast laser pump-probe scheme to design and visualize quantum carpets in the iodine molecule on picometer (pm) and femtosecond (fs) scales.

Figure 1 illustrates our pump-control-probe scheme. The details of the experimental setup are described in EPAPS [33]. Briefly, a jet-cooled thermal-ensemble of the $I_2$ molecules in the $X$ state was irradiated with a pair of phase-locked pump and control laser pulses ($\sim$594 nm, $\sim$110 fs) produced by a homemade highly stabilized Michelson interferometer (attosecond phase modulator; APM) [11,12], and two vibrational WPs composed of $v_B \sim$ 9–16 of the $B$ state were created. The pump-control delay $\tau_{\mathrm{control}}$ was tuned around $1.5T_{\mathrm{vib}}$ ($\sim$470 fs), where $T_{\mathrm{vib}}$ is a classical vibrational period of $I_2$. Hence, two WPs counter-propagated and interfered with each other to weave quantum carpets as is schematically shown in the right panel of Fig. 1. Another fs laser pulse served as a probe pulse used for the laser induced fluorescence measurements of the spatiotemporal images of the carpets. The temporal evolution was measured as a quantum beat by scanning the probe delay $\tau_{\mathrm{probe}}$. According to the classical Franck-Condon (FC) principle, the position of the FC window of this probe step was shifted along the internuclear distance from 330.6 to 336.6 pm as we changed the probe wavelength from 378 to 390 nm [24,25]. During each beat measurement, the delay $\tau_{\mathrm{control}}$ was actively stabilized within $\sim \pm 35$ attoseconds by APM.

For demonstrating the designed carpets, we have chosen four typical pump-control phases $\theta_{\mathrm{pc}}$'s in steps of 90°. The population of each vibrational level within the WPs after the irradiation of the control pulse oscillates with its transition frequency from the initial state as a function of $\tau_{\mathrm{control}}$ because of quantum interference [12]. We have defined the phase origin (0°) as the timing which gives minimum population of the level $v_B = 12$ because this transition stands near the center of the excitation spectrum. With the present optical cycle of the pump and control pulses at 594 nm, the 90° in $\theta_{\mathrm{pc}}$ corresponds to 495 attoseconds in $\tau_{\mathrm{control}}$. The details of the definition of $\theta_{\mathrm{pc}}$ and its uncertainty are described in the EPAPS [33].

Figures 2 (i)–(iii) show the examples of quantum beats measured by scanning $\tau_{\mathrm{probe}}$ with $\theta_{\mathrm{pc}}$ locked to 0° and 180°. The origin $\tau_{\mathrm{probe}} = 0$ denotes a position of the top of the first oscillation in the measured beat with probe wavelength 387 nm in all of the figures shown in the present Letter. The beat signal is highly sensitive to both of the $\theta_{\mathrm{pc}}$ and the probe wavelength. Within the same $\theta_{\mathrm{pc}}$ denoted by the red or blue color in Figs. 2(i)–(iii), the averaged intensity after the control pulse (arrives at $\tau_{\mathrm{probe}} \sim 0.3$ ps) changes drastically as we change the probe wavelength. Similarly, within the same probe wavelength, the averaged intensity changes drastically again between the red and blue traces taken at $\theta_{\mathrm{pc}}$'s different from each other by 180°. The characteristic period of the beat is $0.5T_{\mathrm{vib}}$ in all of the

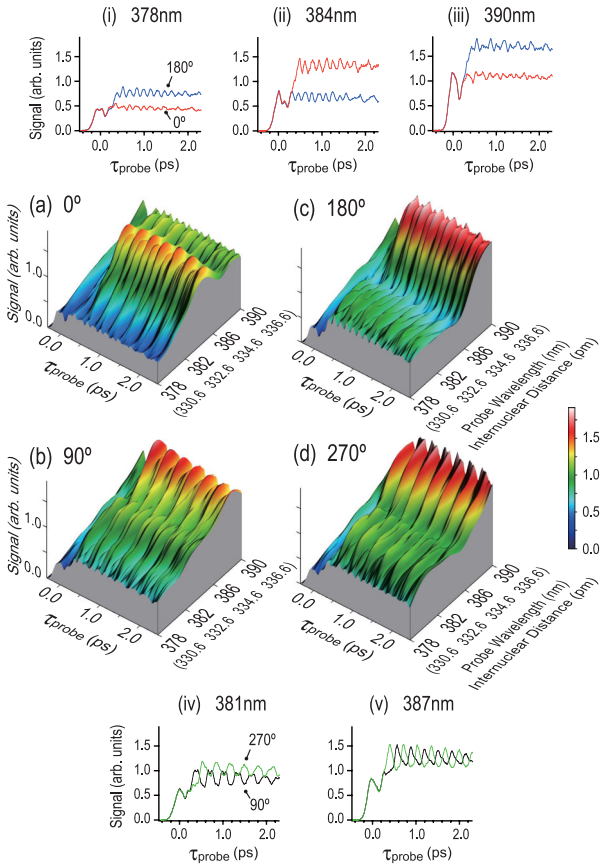


FIG. 2 (color). (a)–(d) Three dimensional (3-D) plots of the fluorescence intensities measured as functions of the pump-probe delay $\tau_{\mathrm{probe}}$ and the probe wavelength with the relative phase $\theta_{\mathrm{pc}}$ of the pump and control pulses tuned to 0°, 90°, 180°, and 270°, respectively. The pump-control delay $\tau_{\mathrm{control}}$ is tuned around $1.5T_{\mathrm{vib}}$ in all cases. (i)–(iii) Examples of the measured fluorescence intensities as functions of $\tau_{\mathrm{probe}}$, which correspond to cross sections of the 3-D plots shown in Figs. 2(a) and 2(c) at the relevant $\theta_{\mathrm{pc}}$'s and probe wavelengths. The red and blue colors denote $\theta_{\mathrm{pc}} = 0°$ and 180°, respectively. (iv)–(v) Similar examples for Figs. 2(b) and 2(d). The black and green curves denote $\theta_{\mathrm{pc}} = 90°$ and 270°, respectively. The details of the data processing are given in the EPAPS [33].

six traces. Similar beat measurements have been made at 9 different probe wavelengths from 378 to 390 nm in steps of $1.5(\pm \sim 0.2)$ nm. These measured beats have been interpolated and plotted as contours to yield 3-D pictures of the quantum carpets shown in Figs. 2(a) and 2(c), where the probe wavelengths are converted to internuclear distances. The details of this conversion and the data analyses are described in EPAPS [33]. It is thus clearly demonstrated that we have succeeded in designing quantum carpets. The most prominent feature seen in comparisons of these two carpets is that the ridge and valley along the $\tau_{\mathrm{probe}}$ axes are interchanged by changing $\theta_{\mathrm{pc}}$ by 180°. Similarly, for $\theta_{\mathrm{pc}}$'s locked to 90° and 270°, Figs. 2(iv) and (v) show the examples of the quantum beats. Again the beat is highly

sensitive to both $\theta_{pc}$ and the probe wavelength; the maxima and minima of the beat are clearly interchanged by changing $\theta_{pc}$ by 180° within the same probe wavelength as well as by changing the probe wavelength from 381 to 387 nm within the same $\theta_{pc}$. The characteristic period of the beat is $T_{vib}$ instead of $0.5T_{vib}$ seen in Figs. 2(i)–(iii). The beats are interpolated and plotted as contours to yield 3-D pictures of quantum carpets in Figs. 2(b) and 2(d), where it is clearly demonstrated that we have created another two designs of the carpets.

Figure 3 shows comparisons of measured and simulated quantum carpets. The theoretical simulations follow the lines as described in Ref. [24], where the pump, control, and probe steps are all included. They also include the vibrational and rotational degrees of freedom and the laser pulse shapes and polarizations. As in Ref. [25], thermal averaging was performed to account for the vibrational and rotational temperatures of the experimental conditions. The general important features are well reproduced by the simulations. The remaining discrepancies can be attributed to the experimental uncertainties in the initial vibrational distribution, imperfections of the laser pulses and to the fact that the transition moments were taken to be constant in the simulations. Since the fringe spacing is given by the de Broglie wavelength, and thus depends on the kinetic energy, it is very sensitive to the exciting laser pulse parameters as well as to the exact initial vibrational distributions. The discrepancies may also be attributed to the detection efficiency possibly different among different probe wavelengths, which may give different wavelengths of the fluorescence signals (see EPAPS [33]). It should be noted that there are three characteristic features associated with the four measured carpets. First, the characteristic temporal period is different between two groups: (i) $\theta_{pc} = 0°$ and 180° and (ii) $\theta_{pc} = 90°$ and 270°; it is $0.5T_{vib}$ for the former group shown in Figs. 3(a) and 3(c), but it is $T_{vib}$ for the latter group shown in Figs. 3(b) and 3(d). Second, the ridge and valley along the $\tau_{probe}$ axis are interchanged between $\theta_{pc} = 0°$ and 180° shown in Figs. 3(a) and 3(c), respectively. A ridge around the internuclear distance $r = 334.0$ pm (~385 nm) in Fig. 3(a) becomes a valley in Fig. 3(c). On the other hand, valleys around $r = 330.6$ pm (378 nm) and 336.6 pm (390 nm) in Fig. 3(a) become ridges in Fig. 3(c). Third, the beat structures are out of phase between two regions in the right and left sides of $r = 334.6$ pm (386 nm) in each of Figs. 3(b) and 3(d), and also out of phase between Figs. 3(b) and 3(d) throughout the whole area. All of these characteristic features are well reproduced in the theoretical simulations, and these agreements confirm our successful carpet design in the present experiments.

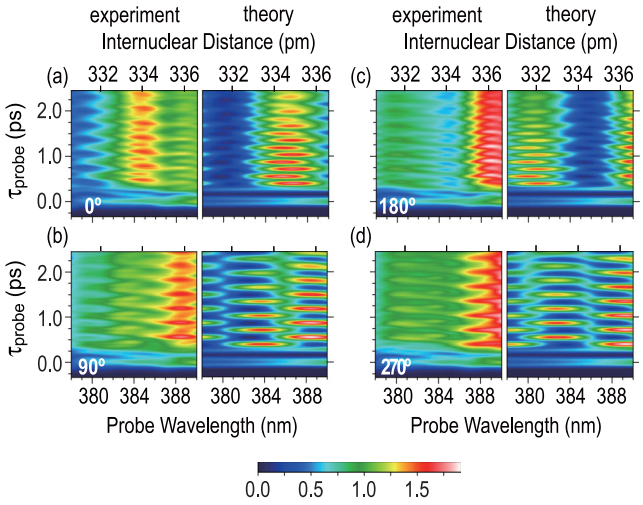


FIG. 3 (color). Comparisons of the quantum carpets measured (left) and simulated (right) at the pump-control relative phases $\theta_{pc}$ = (a) 0°, (b) 90°, (c) 180°, and (d) 270°. The color scaling is common within each set of measured or simulated carpets; the maxima of those two sets have the same color. The origin $\tau_{probe} = 0$ of the simulated carpet denotes a position of the top of the first oscillation around the outer turning point. The simulations include the interactions with the pump, control, and probe pulses. The parameter $\tau_{control}$, used for the simulation of $\theta_{pc} = 0°$ was 468.920 fs.

The first and second features can be attributed to the relative amplitudes of the vibrational eigenfunctions involved in the carpets. Indeed, in the harmonic approximation, the WP can be written (see EPAPS [33])

$$\Psi_{\theta_{pc}}(r, t) = (1 - e^{i\theta_{pc}})\psi_{even}(r, t) + (1 + e^{i\theta_{pc}})\psi_{odd}(r, t), \quad (1)$$

where $\psi_{even}(r, t)$ and $\psi_{odd}(r, t)$ are the partial wave packets composed of the vibrational eigenfunctions with even and odd vibrational quantum numbers, respectively. As can be seen from Eq. (1), the carpets are mainly composed of every second vibrational levels at $\theta_{pc} = 0°$ and 180°, while they include consecutive vibrational levels at $\theta_{pc} = 90°$ and 270° [12]. Consequently, the effective energy spacing of the eigenfunctions is almost twice as large at 0° and 180° as that of 90° and 270°. This explains the double-frequency beats seen in Figs. 3(a) and 3(c). The second feature is also related to the population distribution among the vibrational levels involved in the carpet. The carpets created at $\theta_{pc} = 0°$ and 180° are considered to be mainly composed of the eigenfunctions with odd and even vibrational quantum numbers, respectively [12]. It is reasonable to consider that the positions of the nodes of the even levels almost correspond to the positions of the antinodes of the odd levels, and vice versa. The ridge and valley are thus interchanged between Figs. 3(a) (odd levels) and 3(c) (even levels). From this analysis, it is seen in those figures that the nodes of the odd levels and even levels lie around 330.6 and 336.6 pm and around 334.0 pm, respectively, within the spatial range accessible with the present probe wavelengths.

The third feature is attributed to the relative phases of the vibrational eigenfunctions included in the carpet instead of the relative amplitudes discussed above to elucidate the first and second features. From Eq. (1), the WPs that weave the carpets at 90° and 270° can be written, respectively, as,

$$\Psi_{90}(r,t) \propto (1-i)[\psi_{\mathrm{even}}(r,t) + i\psi_{\mathrm{odd}}(r,t)],$$
$$\Psi_{270}(r,t) \propto (1+i)[\psi_{\mathrm{even}}(r,t) - i\psi_{\mathrm{odd}}(r,t)]. \quad (2)$$

The relative phase of the even levels to the odd levels is thus different by $\pi$ between $\Psi_{90}(r,t)$ and $\Psi_{270}(r,t)$. After temporal evolution for $0.5T_{\mathrm{vib}}$, the relative phase between even and odd levels is shifted by $\sim\pi$ since $T_{\mathrm{vib}}$ is defined in the harmonic approximation to be the time at which adjacent vibrational levels acquire a relative phase of $2\pi$ [12]. It is seen, therefore, that $\Psi_{90}(r, t + 0.5T_{\mathrm{vib}})$ coincides with $\Psi_{270}(r,t)$. The quantum carpet shown in Fig. 3(b) should be completely identical with the one shown in Fig. 3(d) if we shift its origin of $\tau_{\mathrm{probe}}$ by $0.5T_{\mathrm{vib}}$. This is clearly demonstrated in the theoretical simulations. In the actual measurements, however, those two quantum carpets are qualitatively the same with the relevant horizontal shift by $0.5T_{\mathrm{vib}}$; the ridges and valleys are almost superimposed, respectively. But they are not exactly identical. This may be partly because of the slight deviations of $\theta_{\mathrm{pc}}$'s from 90° and 270°, and partly because of the anharmonicity neglected in this discussion.

The quantum carpet is based on the superposition of vibrational eigenfunctions, whose coefficients could be manipulated by a sequence of phase-locked laser pulses. A similar effort has been made by Bucksbaum *et al.* in the case of electronic Rydberg WPs in the Cs atom [4]. In their sophisticated studies, they manipulated a set of amplitudes and phases of electronic eigenfunctions with a pulse shaper, which could subsequently be measured individually. The shape of the Rydberg WP could then be reconstructed by numerical superposition. In our present study, we have directly sculpted and visualized the picometric quantum interference structures.

In conclusion, we have experimentally designed and visualized the quantum carpet woven by ultrafast WP interference in the iodine molecule by using our ultrahigh-precision WPI coupled with the time- and space-sensitive interrogation techniques. The visualized images are resolved on the picometer and femtosecond scales, and its spatiotemporal topology is highly sensitive to the relative amplitudes and phases of vibrational eigenfunctions of which the carpet is composed. As future perspective, the creation of arbitrarily designed quantum patterns is envisaged.

The authors gratefully acknowledge Professor M. Shapiro (Weizmann Inst.), Professor A. Hishikawa (IMS), and Professor R. J. Levis (Temple University) for valuable discussion. This work was partly supported by Grant-in Aid from MEXT of Japan and the French ANR.

*chris@irsamc.ups-tlse.fr
†ohmori@ims.ac.jp

[1] I. Neder *et al.*, Nature (London) **448**, 333 (2007).
[2] Y. Shin *et al.*, Phys. Rev. Lett. **92**, 050405 (2004).
[3] L. Hackermüller *et al.*, Phys. Rev. Lett. **91**, 090408 (2003).
[4] T. C. Weinacht, J. Ahn, and P. H. Bucksbaum, Phys. Rev. Lett. **80**, 5508 (1998); Nature (London) **397**, 233 (1999).
[5] R. R. Jones *et al.*, Phys. Rev. Lett. **71**, 2575 (1993); R. R. Jones, *ibid.* **75**, 1491 (1995).
[6] A. Präkelt *et al.*, Phys. Rev. A **70**, 063407 (2004).
[7] M. W. Noel and C. R. Stroud, Jr., Phys. Rev. Lett. **75**, 1252 (1995); **77**, 1913 (1996); Opt. Express **1**, 176 (1997).
[8] R. E. Carley *et al.*, J. Phys. B **38**, 1907 (2005).
[9] D. Meshulach and Y. Silberberg, Nature (London) **396**, 239 (1998).
[10] A. Monmayrant, B. Chatel, and B. Girard, Phys. Rev. Lett. **96**, 103002 (2006); Opt. Commun. **264**, 256 (2006).
[11] K. Ohmori *et al.*, Phys. Rev. Lett. **96**, 093002 (2006).
[12] H. Katsuki *et al.*, Phys. Rev. A **76**, 013403 (2007).
[13] V. Blanchet, M. A. Bouchene, and B. Girard, J. Chem. Phys. **108**, 4862 (1998).
[14] N. F. Scherer *et al.*, J. Chem. Phys. **95**, 1487 (1991).
[15] Ch. Warmuth *et al.*, J. Chem. Phys. **112**, 5060 (2000); **114**, 9901 (2001).
[16] E. W. Lerch *et al.*, J. Chem. Phys. **124**, 044306 (2006).
[17] M. Fushitani *et al.*, Phys. Chem. Chem. Phys. **7**, 3143 (2005).
[18] T. J. Dunn, I. A. Walmsley, and S. Mukamel, Phys. Rev. Lett. **74**, 884 (1995).
[19] T. S. Humble and J. A. Cina, Phys. Rev. Lett. **93**, 060402 (2004).
[20] J. A. Cina, Annu. Rev. Phys. Chem. **59**, 319 (2008).
[21] M. Wollenhaupt *et al.*, Phys. Rev. Lett., **89**, 173001 (2002).
[22] C. Petersen *et al.*, Phys. Rev. A **70**, 033404 (2004).
[23] I. A. Walmsley and M. G. Raymer, Phys. Rev. A **52**, 681 (1995).
[24] T. Lohmüller *et al.*, J. Chem. Phys. **120**, 10442 (2004).
[25] H. Katsuki *et al.*, Science **311**, 1589 (2006).
[26] O. M. Friesch, I. Marzoli, and W. P. Schleich, New J. Phys. **2**, 4 (2000).
[27] M. Berry, I. Marzoli, and W. P. Schleich, Phys. World **14**, 39 (2001).
[28] M. V. Berry, J. Phys. A **29**, 6617 (1996).
[29] S. Nowak *et al.*, Opt. Lett. **22**, 1430 (1997).
[30] J. Ruostekoski *et al.*, Phys. Rev. A **63**, 043613 (2001).
[31] M. Nest, Phys. Rev. A **73**, 023613 (2006).
[32] L. Deng *et al.*, Phys. Rev. Lett. **83**, 5407 (1999).
[33] See EPAPS Document No. E-PRLTAO-102-080909 for detailed description about the experimental procedures and data analyses. For more information on EPAPS, see http://www.aip.org/pubservs/epaps.html.